

Numerical simulation and experimental validation of multiphysics field coupling mechanisms for a high power ICP wind tunnel

Ming-Hao Yu(喻明浩), Zhe Wang(王哲), Ze-Yang Qiu(邱泽洋), Bo Lv(吕博), and Bo-Rui Zheng(郑博睿)
Citation: Chin. Phys. B, 2021, 30 (**6**): 065201. DOI: 10.1088/1674-1056/abeb0e
Journal homepage: http://cpb.iphy.ac.cn; http://iopscience.iop.org/cpb

What follows is a list of articles you may be interested in

Time-resolved radial uniformity of pulse-modulated inductively coupled O_2/Ar plasmas

Wei Liu(刘巍), Chan Xue(薛婵), Fei Gao(高飞), Yong-Xin Liu(刘永新), You-Nian Wang(王友年), and Yong-Tao Zhao(赵永涛)
Chin. Phys. B, 2021, 30 (**6**): 065202. DOI: 10.1088/1674-1056/abe3f5

Quasi-delta negative ions density of Ar/O_2 inductively coupled plasma at very low electronegativity

Shu-Xia Zhao(赵书霞)
Chin. Phys. B, 2021, 30 (**5**): 055201. DOI: 10.1088/1674-1056/abd16a

Spatio-temporal measurements of overshoot phenomenon in pulsed inductively coupled discharge

Xiang-Yun Lv(吕翔云), Fei Gao(高飞), Quan-Zhi Zhang(张权治), and You-Nian Wang(王友年)
Chin. Phys. B, 2021, 30 (**4**): 045202. DOI: 10.1088/1674-1056/abd16b

Measurement of electronegativity during the E to H mode transition in a radio frequency inductively coupled Ar/O_2 plasma

Peng-Cheng Du(杜鹏程), Fei Gao(高飞, Xiao-Kun Wang(王晓坤), Yong-Xin Liu(刘永新), and You-Nian Wang(王友年)
Chin. Phys. B, 2021, 30 (**3**): 035202. DOI: 10.1088/1674-1056/abccb0

Effect of radio frequency bias on plasma characteristics of inductively coupled argon discharge based on fluid simulations

Xiao-Yan Sun(孙晓艳), Yu-Ru Zhang(张钰如), Sen Chai(柴森), You-Nian Wang(王友年), Yan-Yan Chu(楚艳艳), Jian-Xin He(何建新)
Chin. Phys. B, 2020, 29 (**9**): 095203. DOI: 10.1088/1674-1056/ab9436

Numerical simulation and experimental validation of multiphysics field coupling mechanisms for a high power ICP wind tunnel*

Ming-Hao Yu(喻明浩)[1,†], Zhe Wang(王哲)[1], Ze-Yang Qiu(邱泽洋)[1], Bo Lv(吕博)[1], and Bo-Rui Zheng(郑博睿)[2]

[1] *Faculty of Mechanical and Precision Instrument Engineering, Xi'an University of Technology, Xi'an* 710048, *China*
[2] *School of Automation and Information Engineering, Xi'an University of Technology, Xi'an* 710048, *China*

(Received 21 October 2020; revised manuscript received 8 February 2021; accepted manuscript online 2 March 2021)

We take the established inductively coupled plasma (ICP) wind tunnel as a research object to investigate the thermal protection system of re-entry vehicles. A 1.2-MW high power ICP wind tunnel is studied through numerical simulation and experimental validation. The distribution characteristics and interaction mechanism of the flow field and electromagnetic field of the ICP wind tunnel are investigated using the multi-field coupling method of flow, electromagnetic, chemical, and thermodynamic field. The accuracy of the numerical simulation is validated by comparing the experimental results with the simulation results. Thereafter, the wind tunnel pressure, air velocity, electron density, Joule heating rate, Lorentz force, and electric field intensity obtained using the simulation are analyzed and discussed. The results indicate that for the 1.2-MW ICP wind tunnel, the maximum values of temperature, pressure, electron number density, and other parameters are observed during coil heating. The influence of the radial Lorentz force on the momentum transfer is stronger than that of the axial Lorentz force. The electron number density at the central axis and the amplitude and position of the Joule heating rate are affected by the radial Lorentz force. Moreover, the plasma in the wind tunnel is constantly in the subsonic flow state, and a strong eddy flow is easily generated at the inlet of the wind tunnel.

Keywords: inductively coupled plasma, multiphysics field, coupling mechanism, simulation and experiment

PACS: 52.50.Qt, 52.65.–y, 52.75.Hn, 94.20.Fg **DOI:** 10.1088/1674-1056/abeb0e

1. Introduction

Reconnaissance satellites, manned spacecrafts, and space shuttles should return to the ground in time after they have completed their orbital missions. However, because of their high speed flight, they encounter severe aerodynamic heating problems when they re-enter the dense atmosphere. Accordingly, a perfect thermal protection system is required to ensure the safety of the spacecraft and astronauts. To improve the thermal protection system of re-entry vehicles, an inductively coupled plasma (ICP) wind tunnel is built on the ground for investigating the thermal protection materials for these vehicles.

The ICP wind tunnel can provide flawless long-term stable operation of a high enthalpy plasma jet and accurately simulate the flight environment of re-entry aircraft. It is, therefore, a piece of ideal equipment for investigating the plasma sheath of hypersonic aircraft. The ICP wind tunnel is mainly composed of an intake part, a high frequency discharge part, and a test part. The structural diagram of an ICP wind tunnel is shown in Fig. 1. The high frequency discharge part is mainly comprised of the high frequency power supply, induction coil, and quartz tube. The electrified induction coil is wound around the high temperature resistant quartz tube. After the working gas enters the quartz tube from the air inlet, it is rapidly heated in the induction coil area to form a high temperature high enthalpy induction coupling plasma. The plasma produced in the quartz tube (also called the plasma torch) usually continues to flow forward into the large test chamber. In this chamber, the ICP can be used to test the aerodynamic performance of the aircraft, develop thermal protection materials[1] and investigate communication blackouts and electromagnetic wave transmissions.[2]

The ICP has been widely utilized in aerospace, materials, chemical industry, and other fields since the 1960s and 1970s. Presently, with rapid industrial development, many researchers have performed experiments and numerical simulations on ICPs.[1–5] In an experimental research, Moon *et al.*[4] measured the plasma density and coil voltage in ICP by using floating and high voltage probes, respectively, and studied the influence of coil turns on the ICP. They found that the plasma density increased with the number of coil turns because of the enhancement of inductive coupling. Moreover, the coil voltage was affected by both the plasma density and the coil. Their research can considerably aid the design of future ICP sources. Kim *et al.*[5] performed experiments on a CO_2 ICP that had a pressure of 100 mTorr (1 Torr = 1.33322×10^2 Pa) and power

*Project supported by the National Natural Science Foundation of China (Grant No. 11705143), the Open Foundation for Key Laboratories of National Defense Science and Technology of China (Grant No. 6142202031901), and the Foundation for Research and Development of Applied Technology in Beilin District of Xi'an, China (Grant No. GX2047).

†Corresponding author. E-mail: ymh@xaut.edu.cn

© 2021 Chinese Physical Society and IOP Publishing Ltd

of 13.56 MHz. Electron energy distribution functions were measured using a Langmuir probe, and other plasma parameters, such as electron number density and electron temperature, were also obtained. According to the electrostatic probe technology, Pan *et al.*[6] developed an electrostatic probe diagnosis system suitable for the test environment of a high frequency plasma wind tunnel. This system was employed to diagnose the flow field parameters of the ICP wind tunnel. Fujita *et al.*[7] measured the temperature parameters of plasma in an ICP wind tunnel by means of a radiation spectrum.

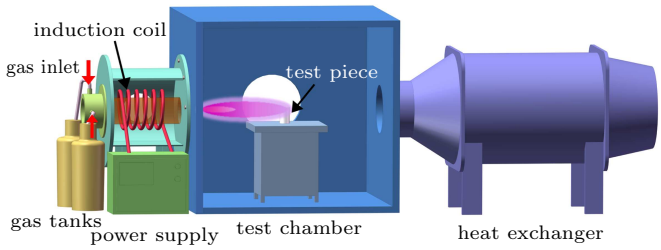


Fig. 1. Structural diagram of inductively coupled plasma wind tunnel.

Regarding the numerical studies of the ICPs, Ivanov and Zverev[8] numerically studied the influence of hydrogen on the parameters of plasma in the ICP torch with considering chemical reactions of Ar with H_2. They found that as the hydrogen percentage increases over 10% at a constant total $Ar + H_2$ mass flow rate, the electrical conductivity of plasma increases slightly, but the enthalpy of plasma increases significantly due to high value of the dissociation energy of hydrogen molecules. Degrez *et al.*[9] also numerically studied the air ICP under a local thermodynamic equilibrium and a chemical non-equilibrium. They provided the calculation results of the streamline, temperature, and chemical concentration field in the air ICP torch. Alavi and Mostaghimi[10] numerically and experimentally studied a novel ICP torch which possesses a conical nozzle. The inductive coil were wound around the conical nozzle rather than around the conventional quartz tube. They found that the new torch has higher power density, better plasma stability, and better resistance against extinguishing factors than the traditional torch. Nam *et al.*[11] conducted a numerical analysis of the power distribution and heat flow characteristics of Ar–N_2 ICP with nitrogen content of 0 mol%–50 mol% at a plasma power level of 50 kW. They obtained relevant data, such as heat loss and load resistance. They also employed numerical simulation and equivalent circuit analysis to optimize the design and analysis of a high power ICP torch system with a vacuum tube oscillator. Lu and Feng[12] investigated the effects of the operating parameters on the ICP properties by a non-equilibrium magnetohydrodynamic model. Their numerical model can aid in determining the optimal conditions for producing the ideal plasma. Sun *et al.*[13,14] studied ICP plasma characteristics by using two-dimensional self-consistent fluid model. It was found that the spatial distribution of plasma characteristics was controlled by changing the bias power of single frequency bias or high frequency bias power ratio of double frequency offset. The plasma density and ion species ratio were adjusted by changing bias voltage and pulse frequency. Gao *et al.*[15] found that different RF bias voltage has different effect on plasma characteristics: in the low RF voltage range, the electron number density decreases and the effective electron temperature increases; in the high RF voltage range the electron number density increases and the effective electronic temperature decreases.

In addition, with the rapid development of commercial softwares such as ANSYS, COMSOL, *etc*., many research groups prefer to simulate the ICP using these as simulation tools. For example, Zhu *et al.*[16] used the ANSYS FLUENT software to simulate a two-dimensional ICP torch and derived the electromagnetic field distribution, temperature distribution, and velocity distribution in the torch. Chen *et al.*[17] employed the ANSYS FLUENT software to calculate the temperature of pure argon thermal plasma and the flow field distribution in the plasma generator device. They found that the temperature distribution and flow field distribution can be controlled by changing the corresponding device structure and working frequency. Zhao[18] established a fluid model of argon ICP by using the COMSOL software. It was observed that the temperature of the argon ICP changed non-monotonically with power. To explain this phenomenon, a new equation for the average electron energy was proposed. Lei *et al.*[19] employed the COMSOL software to simulate the ICP discharge and studied the influences of different coil designs and gas compositions on the discharge characteristics of a two-dimensional ICP. The best discharge characteristic is considered to be afforded by a 20-mm coil gap, with the first coil positioned 130 mm away from the top of the device, and the best discharge mode is considered to be argon discharge mode. This numerical model is a typical ICP discharge, and its results are important for further experimental studies.

Although the above-mentioned research groups have conducted in-depth research on the numerical simulation of ICP, the majority of their simulation results have not been validated experimentally. Moreover, most of researches focused on low power (1 kW–50 kW) ICP wind tunnels. There is a lack of detailed studies to reveal the flow characteristics and the multi-physics coupling mechanism of the high power (such as a 1.2-MW class) ICP wind tunnel. For example, on the one hand, for a low power ICP wind tunnel,[20–23] its coil current, working pressure, plasma density are usually small;[20–22] hence, its electromagnetic field is small,[22,23] and the coupling effect between the electromagnetic field and the flow field is also relatively weak. One the other hand, for a high power ICP wind tunnel,[24,25] its working parameters such as the in-

put power, operating pressure and the discharge frequency are quite different from those for a low power ICP wind tunnel. Its plasma density, electric-field intensity, plasma temperature, and heat flux are all higher than those of the low power one.[26,27] Thus, for the high power ICP wind tunnel, the coupling effects among the electromagnetic, flow, chemical, and thermodynamic fields are much stronger and more complex. Therefore, further researches on the high power ICP wind tunnel should be conducted to make clear such complex coupling effects. While so far there has been few such work available.

In the present study, a 1.2-MW high power ICP wind tunnel is studied as a research object. Furthermore, the coupling mechanisms of the electromagnetic field, flow field, chemical field, and thermal field of the wind tunnel are explored and discussed by combining numerical simulation with experimental validation. The electron number density, temperature, pressure, electric field intensity, Lorentz force, and other important parameters are discussed and investigated through numerical simulation. The plasma parameters under different working conditions are compared with each other to reveal the distribution characteristics of the flow field, electromagnetic field, chemical field, and thermal field of the high power wind tunnel. The accuracy of the numerical simulation is verified by comparing the simulation results with experimental data.[24]

In the following sections, the computational grid, operating conditions, control equations, numerical solution methods, and boundary conditions of the high power ICP wind tunnel are presented. Thereafter, by analyzing the distribution of flow field parameters (*e.g.*, temperature, electron density, and pressure) and electromagnetic field parameters (*e.g.*, electric field intensity and Lorentz force) of the ICP wind tunnel under two different power values, the interaction and influence mechanism between the flow field and electromagnetic field in the high power ICP wind tunnel are determined. Finally, the accuracy of the research results is verified by comparing the experimental results with the numerical results.

2. Research methods

The research object of this study is an ICP wind tunnel with a power of up to 1.2 MW. The plasma torch is made of a quartz tube with an inner diameter and a wall thickness of 80 mm and 3 mm, respectively; six electrified coils are wound around this tube. As shown in Fig. 2, the calculation domain of the electromagnetic field is $-100\ \text{mm} \le x \le 570\ \text{mm}$ and $0\ \text{mm} \le y \le 450\ \text{mm}$, with each interval consisting of 161×97 grid nodes; the ICP torch consists of 111×41 grid nodes. The whole flow field grids including the vacuum chamber are composed of 329×41 nodes as shown in Fig. 3.

To calculate the electromagnetic field near the coil and air velocity at the air inlet accurately, the calculation grid is encrypted in both the area of the induction coil and the area of inlet. In this study, it is assumed that the plasma is steady, electrically quasineutral and two-dimensionally axisymmetric. The fluid micro-element is in a thermochemical non-equilibrium state. In the simulation calculation, the Lorentz force and induced magnetic field generated by the plasma are considered.

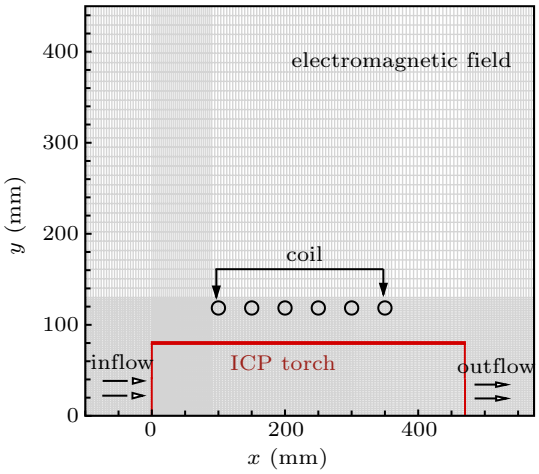


Fig. 2. Computational mesh of electromagnetic-field and ICP torch.

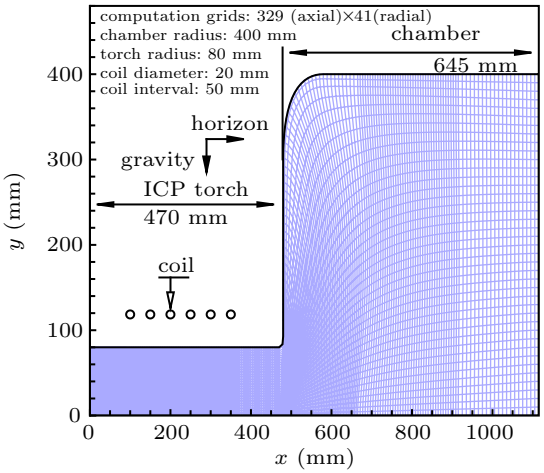


Fig. 3. Computational mesh of the whole flow field.

Usually, the plasma discharge is ignited by an appropriate argon injection and thereafter, gradually replaced by an air mixture (16 g/s standard dust-free atmospheric air) until stable working conditions are reached. To measure the temperature of plasma particles, spectrum analyzers are located at 195, 320, and 445 mm away from the plasma torch outlet. For the simulation study, two typical working conditions: cases 1 and 2 for the 1.2-MW ICP wind tunnel are selected. The specific working conditions are listed in Table 1. The influences of different working conditions on the plasma temperature, velocity, pressure, electron density, electric field intensity, and other parameters are compared to demonstrate the flow field and electromagnetic field distribution characteristics of the high power ICP wind tunnel. These comparisons are based on the multi-field coupling solutions of the flow field, electromagnetic field, thermodynamic field, and chemical field.

Table 1. Working conditions of computational cases.

Cases	Input power $P_{\rm el}$ (kW)	Pressure p (Pa)	Inflow mass flow rate m (g/s)	Working gas	Frequency of current f (MHz)
1	160	15000	16	air	0.4
2	200	15000	16		
3	160	10000	16		
4	200	10000	16		

2.1. Governing equations

The vector form of the system of non-equilibrium magnetohydrodynamic equations is as follows:

$$\frac{\partial \boldsymbol{Q}}{\partial t}+\frac{\partial \boldsymbol{F}}{\partial x_j}=\frac{\partial \boldsymbol{F}_{\boldsymbol{v}}}{\partial x_j}+\boldsymbol{W}. \tag{1}$$

The gas temperature consists of the translational temperature ($T_{\rm tr}$), rotational temperature ($T_{\rm rot}$), vibration temperature ($T_{\rm vib}$), and electronic temperature ($T_{\rm e}$). The conservation vector $\boldsymbol{Q}$, flux vectors $\boldsymbol{F}$ and $\boldsymbol{F}_{\boldsymbol{v}}$, and source term vector $\boldsymbol{W}$ in Eq. (1) are expressed as follows:

$$\boldsymbol{Q}=\begin{bmatrix}\rho\\ \rho u_i\\ E\\ \rho_s\\ E_{\rm rot}\\ E_{\rm vib}\\ E_{\rm e}\end{bmatrix},\quad \boldsymbol{F}=\begin{bmatrix}\rho u_j\\ \rho u_i u_j+\delta_{ij}p\\ (E+p)u_j\\ \rho_s u_j\\ E_{\rm rot}u_j\\ E_{\rm vib}u_j\\ E_{\rm e}u_j\end{bmatrix},$$

$$\boldsymbol{F}_{\boldsymbol{v}}=\begin{bmatrix}0\\ \tau_{ij}\\ q_j+\rho\sum\limits_{s=1}^{ns}h_sD_s\dfrac{\partial X_s}{\partial x_j}+u_i\tau_{ij}\\ \rho D_s\dfrac{\partial X_s}{\partial x_j}\\ q_{{\rm rot},j}+\rho\sum\limits_{s=M}e_{{\rm rot},s}D_s\dfrac{\partial X_s}{\partial x_j}\\ q_{{\rm vib},j}+\rho\sum\limits_{s=M}e_{{\rm vib},s}D_s\dfrac{\partial X_s}{\partial x_j}\\ q_{{\rm e},j}+\rho h_{\rm e}D_{\rm e}\dfrac{\partial X_{\rm e}}{\partial x_j}-p_{\rm e}u_j\end{bmatrix},$$

$$\boldsymbol{W}=\begin{bmatrix}0\\ F_{{\rm L}i}+G_i\\ S_{\rm joule}\\ \dot{\omega}_s\\ S_{\rm int,rot}\\ S_{\rm int,vib}\\ S_{\rm joule}+S_{\rm int,\,e}\end{bmatrix}, \tag{2}$$

where $\delta_{i,j}$, $F_{{\rm L}i}$, $S_{\rm joule}$, $S_{\rm int}$, Δh_s^0, and $\Theta_{{\rm vib},s}$ denote the Kronecker function, Lorentz force, Joule heating efficiency, internal energy exchange rate, component formation enthalpy, and vibration characteristic temperature, respectively; subscript s represents the chemical species; M is the molecular number; $\dot{\omega}_s$ is the mass generation rate of substance s and is the source term of the mass conservation equation of the particle at line 4 in $\boldsymbol{W}$, X_s, and D_s are the mole fraction and diffusion coefficient of s, respectively; u_i (or u_j) and x_j represent the velocity and tensor in the rectangular coordinate system, respectively; τ_{ij} and q_j are the stress tensor and the heat flux vector, respectively, and expressed as

$$\tau_{ij}=\mu\left(\frac{\partial u_i}{\partial x_j}+\frac{\partial u_j}{\partial x_i}-\frac{2}{3}\frac{\partial u_k}{\partial x_k}\delta_{ij}\right), \tag{3}$$

$$\begin{aligned}q_j&=q_{\rm tr,j}+q_{{\rm rot},j}+q_{{\rm vib},j}+q_{{\rm e},j}\\ &=\lambda_{\rm tr}\frac{\partial T_{\rm tr}}{\partial x_j}+\lambda_{\rm rot}\frac{\partial T_{\rm rot}}{\partial x_j}+\lambda_{\rm vib}\frac{\partial T_{\rm vib}}{\partial x_j}+\lambda_{\rm e}\frac{\partial T_{\rm e}}{\partial x_j}.\end{aligned} \tag{4}$$

The high temperature gas pressure (p) is calculated from the gas state equation as follows:

$$p=\sum_{s\neq e}^{ns-1}\rho_sR_sT_{\rm tr}+\rho_eR_eT_e=\rho\hat{R}T_{\rm tr}+p_e. \tag{5}$$

The total internal energy (E) of the gas is defined as follows:

$$\begin{aligned}E&=E_{\rm tr}+E_{\rm rot}+E_{\rm vib}+E_{\rm e}+\sum_{s=1}^{ns}\rho_s\Delta h_s^0\\ &\quad+\frac{1}{2}\rho u_iu_i+\frac{3}{2}\rho k.\end{aligned} \tag{6}$$

The translational energy ($E_{\rm tr}$), rotational energy ($E_{\rm rot}$), vibration energy ($E_{\rm vib}$), and electronic internal energy ($E_{\rm e}$) of gas particle are calculated by the corresponding equations given in the work of Yu *et al.*[22]

The gas viscosity μ, and translational $\lambda_{\rm tr}$, vibrational $\lambda_{\rm vib}$, rotational thermal conductivity $\lambda_{\rm rot}$ in the above equations are all computed from Yos' formulas.[28,29] The diffusion coefficient D_s is calculated from the formula of Curtiss and Hirschfelder.[30] The conductivity of plasma σ and the electron thermal conductivity $\lambda_{\rm e}$ are evaluated from the third-order Sonine polynomials of air.[31–33]

The Joule heating rate $S_{\rm joule}$, and the axial and radial Lorenz force, *i.e.*, $F_{{\rm L}x}$ and $F_{{\rm L}y}$ can be calculated from the following equations, respectively:

$$S_{\rm joule}=\frac{1}{2}\sigma\left(E_{\rm R}^2+E_{\rm I}^2\right). \tag{7}$$

$$F_{{\rm L}x}=\frac{\sigma}{2\omega}\left(E_{\rm I}\frac{\partial E_{\rm R}}{\partial x}-E_{\rm R}\frac{\partial E_{\rm I}}{\partial x}\right), \tag{8}$$

$$F_{{\rm L}y}=-\frac{\sigma}{2\omega}\left(E_{\rm R}\frac{\partial E_{\rm I}}{\partial y}-E_{\rm I}\frac{\partial E_{\rm R}}{\partial y}\right). \tag{9}$$

Here, $E_\theta=E_{\rm R}+{\rm i}E_{\rm I}$. $E_{\rm R}$ and $E_{\rm I}$ are the real and imaginary part of the electric field intensity, respectively.

They are obtained by solving the magnetic vector-potential equations[22] at each time step.

In addition, in Eq. (2), the rotational energy exchange rate ($S_{\mathrm{int,rot}}$), vibration energy exchange rate ($S_{\mathrm{int,vib}}$), and electron energy exchange rate ($S_{\mathrm{int,e}}$) are calculated from the following equations:

$$S_{\mathrm{int,rot}} = Q_{\mathrm{T-R}} - Q_{\mathrm{R-V}} - Q_{\mathrm{R-e}} + Q_{\mathrm{D}}^{\mathrm{rot}}, \tag{10}$$

$$S_{\mathrm{int,vib}} = Q_{\mathrm{T-V}} + Q_{\mathrm{R-V}} + Q_{\mathrm{e-V}} + Q_{\mathrm{D}}^{\mathrm{vib}}, \tag{11}$$

$$S_{\mathrm{int,e}} = Q_{\mathrm{T-e}} + Q_{\mathrm{R-e}} - Q_{\mathrm{e-V}} + Q_{\mathrm{D}}^{\mathrm{e}} + Q_{\mathrm{I}}^{\mathrm{e}}, \tag{12}$$

where $Q_{\mathrm{T-R}}$ is the translation energy–rotation energy exchange rate; $Q_{\mathrm{R-V}}$ is the rotation energy–vibration energy exchange rate; $Q_{\mathrm{R-e}}$ is the rotation energy–electron energy exchange rate; $Q_{\mathrm{T-V}}$ is the translation energy–vibration energy exchange rate; $Q_{\mathrm{e-V}}$ is the electron energy–vibration energy exchange rate; $Q_{\mathrm{T-e}}$ is the translation energy–electron energy exchange rate; $Q_{\mathrm{D}}^{\mathrm{rot}}$, $Q_{\mathrm{D}}^{\mathrm{vib}}$, $Q_{\mathrm{D}}^{\mathrm{e}}$, and $Q_{\mathrm{I}}^{\mathrm{e}}$ are the energy losses of air molecules because of the dissociation reaction and ionisation reaction.

In order to reproduce the chemical reactions of air plasmas, the chemical kinetic model, which includes 11 species (N_2, O_2, NO, N_2^+, O_2^+, NO^+, N, O, N^+, O^+, e^-) and 54 chemical reactions,[34] is employed in the present study. The forward and backward reaction rate are calculated from the Arrhenius formula.[35] Finally, the mass production rate of an air component, s, due to a chemical reaction, r (Here 's' denotes one of species in 11 air species, 'r' refers to one of chemical reactions in 49 air chemical reactions) can be calculated from the following formula:

$$\dot{\omega}_s = M_s \sum_{r=1}^{nr} \left(\nu_s^{b,r} - \nu_s^{f,r}\right) \times \left[k_{f,r} \prod_{j=1}^{ns} \left(\frac{\rho_j}{M_j}\right)^{\nu_{j,r}} - k_{b,r} \prod_{j=1}^{ns} \left(\frac{\rho_j}{M_j}\right)^{\nu'_{j,r}}\right]. \tag{13}$$

Here, $\nu_s^{b,r}$ and$\nu_s^{f,r}$ are the stoichiometric coefficient of component$s$ before and after the r chemical reaction, respectively; M_s represents the molar mass of substance s; s and j are the subscripts representing the component numbers of chemical species. The mass production rate of species s, *i.e.*, $\dot{\omega}_s$ acts as a mass source term in the mass conservation equation of chemical species in the fourth row of the source term $\boldsymbol{W}$ in Eq. (2). It participates in iterative computations of the non-equilibrium magnetohydrodynamic equations mentioned above, and updates solutions at each time step.

2.2. Iterative computational methods

To iteratively solve the governing equations mentioned above, the flow field equations are discretized by the finite-volume method. The viscous term is calculated by the second-order center difference method. To compute the inviscid fluxes of the flow field equations at the cell interfaces, the simple low dissipation advection upwind[36] (SLAU) splitting method, which is a parameter-free and simple compressible numerical flux function of the AUSM family method, is used. The monotonic upstream-centered scheme for conservation law (MUSCL).[37,38] is adopted to avoid computational oscillations and spurious solutions in the region of high gradients. In the presently-used MUSCL, the physical properties at the cell interface are determined by linearly interpolating properties between neighboring cells. Thus, the accuracy of the inviscid numerical flux is kept to the second order. To overcome the numerical stiffness for a chemical nonequilibrium plasma, the point-implicit method[39] is utilized in this study. In addition, the point-implicit lower and upper symmetric Gauss–Seidel (LU-SGS) method[40] is used to update the solutions of the flow field results at each time step.

The finite-difference method is adopted to discretize the magnetic vector-potential equations to figure out the distributions of the electric field intensities E_{R} and E_{I}. The second-order, central-difference method is used to evaluate their numerical flux. The sub-relaxation iterative method is used to solve the discretized electromagnetic-field equations stably. The relaxation factor is set to be 0.5. When the relative error of the magnetic-vector potential between n and $n+1$ steps is less than 10^{-5}, the calculation is considered to be converged.

In this study, the local time stepping scheme is adopted to update the flow field results. When the residual of the mass, the momentum and the energy conservative equation are less than 10^{-5}, 10^{-5}, and 10^{-3}, respectively, then the simulation is thought to be converged. In the present study, because the chemical nonequilibrium process of the chemical reaction of air is considered and modeled in the simulation, the residual of the energy conservative equation can hardly reach 10^{-5}. Thus, when the residual of the energy conservative equation reaches 10^{-3} and the flow parameters such as the temperature, velocity and pressure are no more changed after 1.2 million iterative computational steps, then we think the simulation is converged. In addition, all the equations and models mentioned above are programmed by the computer language Fortran 90 by ourselves. The computational mesh of the ICP wind tunnel is divided by Gridgen V15. All simulations are carried out by using the Tianhe-2 Supercomputer.

2.3. Boundary conditions

The working gas is injected into the quartz tube; the mass flow rate and initial gas temperature are $m = 16$ g/s and $T_0 = 300$ K, respectively. At the exit of the ICP wind tun-

nel laboratory, the working pressure is set to be a fixed value, and other flow properties are evaluated through the linear interpolation of adjacent internal grid points. For the central axis, the axisymmetric boundary condition ($Q_{i,j} = Q_{i,j+1}$) is adopted, where Q denotes the conservation variable. For the magnetic vector-potential equations, the outer boundary of the electromagnetic field calculation area is set to be $x = -10$, $x = 570$, and $y = 450$ mm. The electric field intensities E_R and E_I are set to be zero at these outer boundaries: $E_{i,0} = E_{i,1}$. It is assumed that there is no slippage nor catalytic effect nor pressure gradient on the wall of the plasma torch. The wall temperature is determined using the heat conduction equation, $\partial T_w/\partial n = q_{j\max}$, where $q_{j\max}$ is the heat flux density at the inner wall. For the wall in the test room, a constant wall temperature boundary condition is adopted, *i.e.*, $T_w = 300$ K.

3. Results and discussion

3.1. Numerical results

In this subsection, we will show the simulated results of flow, electromagnetic, and chemical fields, respectively. As is well known, when the input power is different, the flow properties such as the pressure, temperature, velocity also change and may demonstrate different physical results. So in order to make clear this issue for the high power ICPWT, we take case 1 and case 2 listed in Table 1 as baseline cases to show the flow field differences under the different input power conditions. The simulated results of these two cases will be discussed comparatively below.

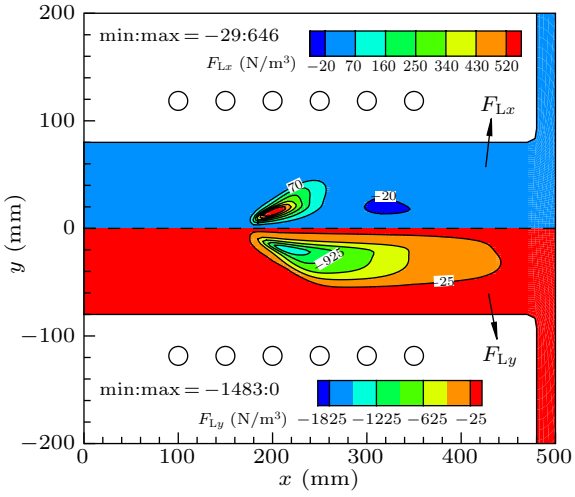


Fig. 4. Distribution of axial Lorentz force (upper half) and radial Lorentz force (lower half) for case 1.

Figures 4 and 5 show the distributions of the axial and radial Lorentz forces in the plasma torches for case 1 and case 2, respectively. First, it can be observed that the maximum axial and radial Lorentz force position are under the third coil and fourth coil, respectively. The axial Lorentz forces in both cases are positive and negative, whereas the radial Lorentz forces are both always negative. The radial Lorentz force direction is from the wall to the central axis. Second, the maximum values of the radial Lorentz force are 2.23 and 3.05 times greater than the maximum values of the axial Lorentz force for case 1 and case 2, respectively. This proves that the radial momentum transfer of the plasma is stronger than the axial momentum transfer. Finally, because the greater the input power, the greater the electric field intensity and Lorentz force are. Hence, the Lorentz force for case 2 is greater than that for case 1.

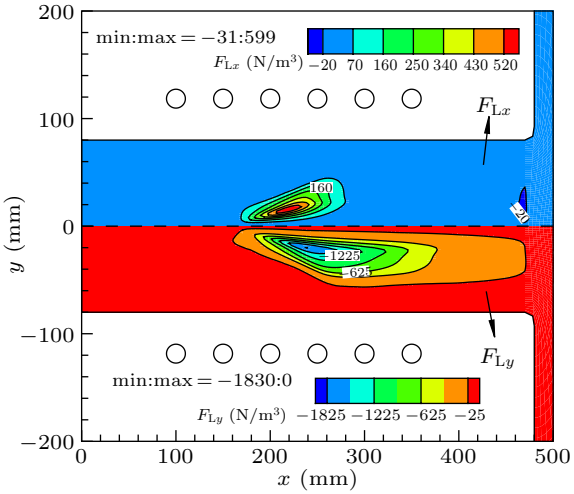


Fig. 5. Distribution of axial Lorentz force (upper half) and radial Lorentz force (lower half) for case 2.

Figures 6 and 7 show the distribution diagrams of the electronic number density and imaginary part of the electric-field intensity in the plasma torch for case 1 and case 2, respectively. The electronic number density and electric field intensity considerably vary in the plasma torch, and their maximum value positions are under the third and fourth coil, respectively. The upper half of the figure shows that the electron number density is maximum at the central axis and minimum at the wall. This is because the radial Lorentz force is negative, and its direction points from the wall to the central axis. The electrons are gathered at the central axis under the action of the radial Lorentz force. The maximum electron number densities for cases 1 and 2 are 1.01×10^{22} m^{-3} and 9.05×10^{21} m^{-3}, respectively. The lower half for each of the figures shows that the maximum negative electric-field intensity is on the plasma torch wall and gradually decreases away from the wall. The maximum electric-field intensity in case 2 is greater than that in case 1. This is because a negative electric field is generated by the current of the external induction coil; it is maximum near the wall and minimum near the central axis. The positive electric field generated by the plasma is the largest near the central axis; it can offset part of the negative electric field. The electric field intensity in case 2 is greater than that in case

1, because the input power of the coil in case 2 is greater than that in case 1.

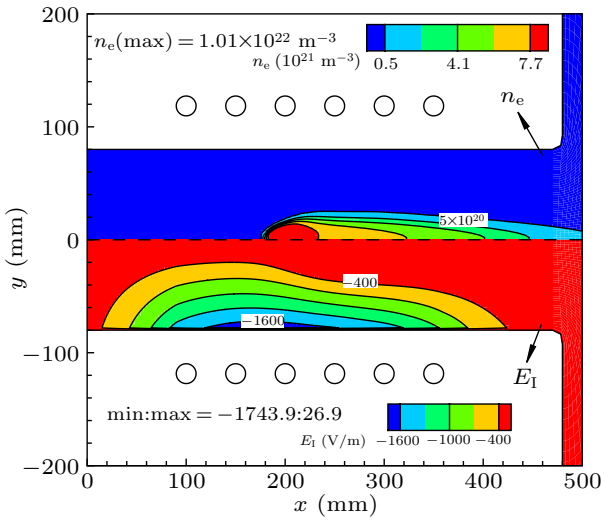


Fig. 6. Distribution of electron number density (upper half) and imaginary part of electric-field intensity (lower half) for case 1.

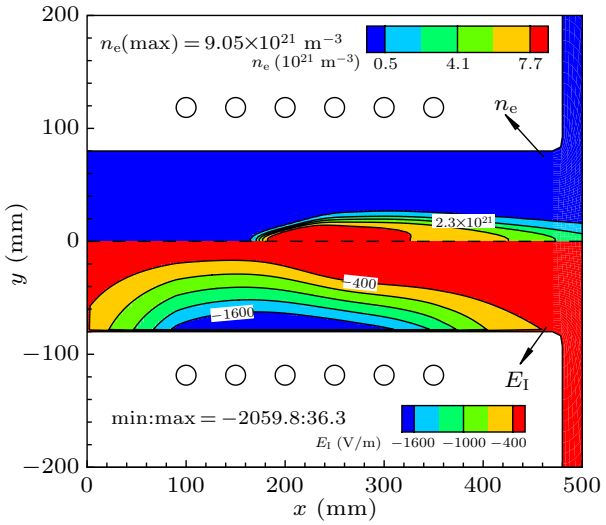


Fig. 7. Distribution of electron number density (upper half) and imaginary part of electric-field (lower half) for case 2.

Figures 8 and 9 show the distribution of the Joule heating rate and radial Lorentz force in the plasma torch for case 1 and case 2, respectively. The electromagnetic field and flow field of the wind tunnel are coupled and connected through the Joule heating rate and Lorentz force. First, it is observed that the distribution shape of the Joule heating rate is similar to that of radial Lorentz force, and the maximum value positions of Joule heating rate are also below the third and fourth coil. This proves that the position of the Joule heating phenomenon is mainly governed by the radial Lorentz force. Second, according to the formula, the Joule heating rate is directly proportional to the electric field intensity. Figures 6 and 7 show that the maximum electric field intensity is close to the wall, whereas the maximum Joule heating rate is not on the wall but approximately 40 mm away from the wall. This is because a cooling device is used for the wall of the plasma torch, thereby reducing the Joule heating rate. The power in case 2 is greater than that in case 1. According to the proportional relationship between power and electric field intensity, the greater the electric power, the greater the electric field intensity and the Joule heating rate are. The maximum Joule heating rate in cases 1 and 2 are 7.0×10^7 W/m^3 and 8.2×10^7 W/m^3, respectively.

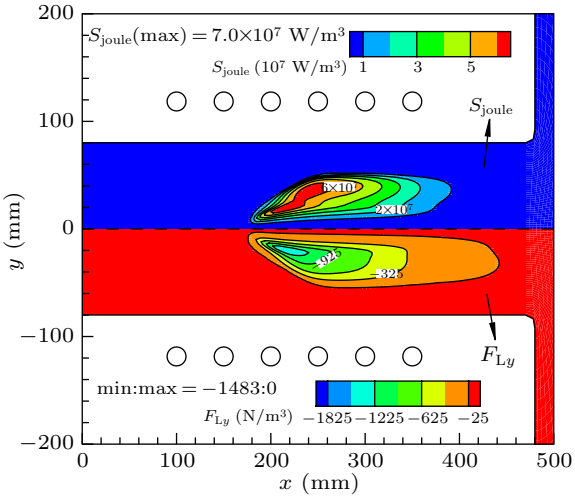


Fig. 8. Distribution of Joule heating rate (upper half) and radial Lorentz force (lower half) for case 1.

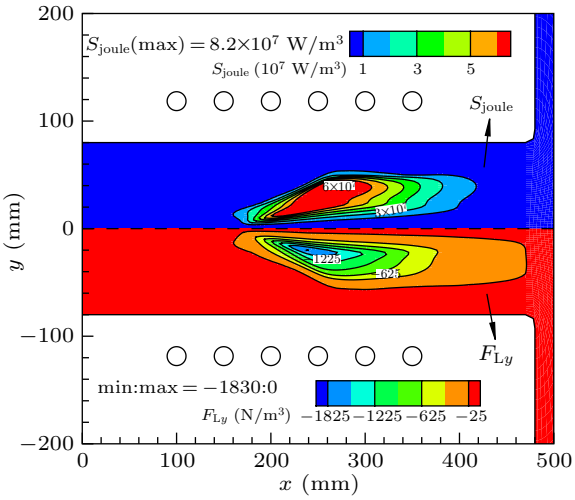


Fig. 9. Distribution of Joule heating rate (upper half) and radial Lorentz force (lower half) for case 2.

Figures 10 and 11 show the streamline and velocity distribution in the entire flow field for case 1 and case 2, respectively; it can be observed that the maximum velocity in case 1 and case 2 are 110 m/s and 129 m/s, respectively. The maximum plasma flow velocity is found to be at the torch outlet. The maximum of flow velocity is on the central axis, and its minimum is on the test chamber wall. In the plasma torch, a strong vortex can be observed from the gas inlet to the second coils in Fig. 11. Such one or two recirculation flows are frequently found in the ICP simulations.[22,26,41] It has been reported that this vortex results mainly from the effect of the Lorentz force and the negative pressure gradient[22] generated in the coil region (see Figs. 12 and 14 below). On the one hand, the radial and axial component of the Lorentz force can

affect corresponding momentum transfer of charged species significantly for a plasma flow. The strong radial Lorentz force strengthens the pinch effect, which can narrow the radial electrical channel of electrons and squeeze the plasma flow in the radial direction in the coil region.[22] On the other hand, both the negative axial Lorentz force and the negative pressure gradient beneath the inductive coils act as resistive forces to prevent the plasma flow from moving forward smoothly. As a result, some of the plasma elements move backwards and form a vortex near the center axis in the coil region.

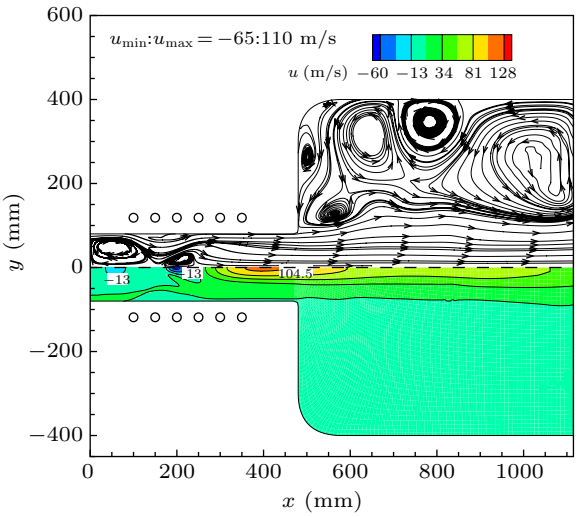


Fig. 10. Distribution of streamlines (upper half) and velocity (lower half) for case 1.

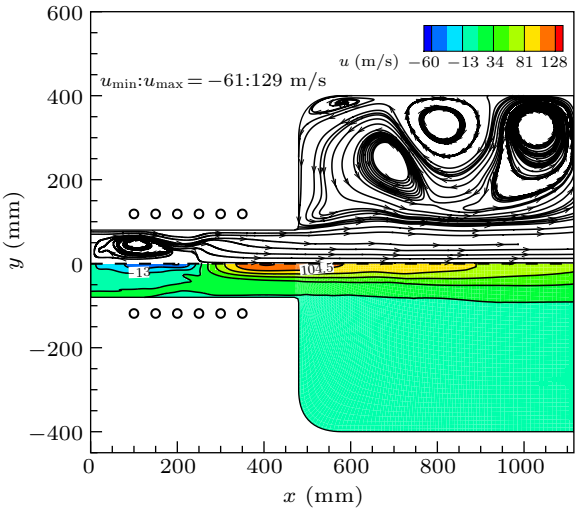


Fig. 11. Distribution of streamlines (upper half) and velocity (lower half) for case 2.

In addition, near the wall of the test chamber, there are several notable vortexes. Their formation and intensity are affected mainly by the pressure characteristics of the spacious vacuum chamber. First, due to the high speed plasma flowing along the center axis from the torch outlet to the test chamber outlet, it will results in pressure differences between the chamber wall and the outer boundary of the plasma column in the spacious test chamber. The local pressure difference in a spacious chamber easily results in recirculation flow in the chamber. While such recirculation flows near the chamber wall hardly affect the flow properties of the plasma column near the center axis due to the far distance.

To check the correctness of the velocity simulated in our study, we consult several relevant references.[12,25,42] Approximate values of the simulated velocity are found for the high power ICPs.[25,42] For example, Vasil'evskii and Kolesnikov[25] simulated an air ICP flow under similar working conditions: the nominal input power $P = 90$ kW, $f = 0.44$ MHz, $p = 10$ kPa, $m = 2.8$ g/s. Their simulated maximum velocity at the torch exit is about 150 m/s.[25] Although their input power is lower than $P = 160$ kW in our case 1, their working pressure and mass flow rate are also lower than $p = 15$ kPa, $m = 16$ g/s in case 1, respectively. Lu and Feng[12] has reported that the plasma velocity decreases as the pressure and the mass flow rate increase. Thus, for case 1 the simulated maximum velocity (110 m/s) has the same order of magnitude as the one (150 m/s) reported by Vasil'evskii and Kolesnikov.[25] Thus, the maximum plasma velocities obtained in our simulations are reasonable.

Figures 12–14 show the distributions of the static pressure for case 1 and case 2. The maximum pressure positions are both below the third and fourth coil. The maximum pressures for cases 1 and 2 are 15027.9 Pa and 15076.7 Pa, respectively; thus, the maximum pressure for case 2 is greater than that for case 1. From Fig. 14 it follows that the pressure variation trends of these two cases are similar along the center axis, Along the positive direction of the x axis, the pressure value under the induction coil first increases and then decreases until the pressure value tend to be an identical constant of approximately 1.5×10^4 Pa in the test chamber for these two computational cases. However, for these two cases, their maximum pressure drops in the whole flow field are 27.9 Pa and 76.7 Pa, respectively. They are both small.

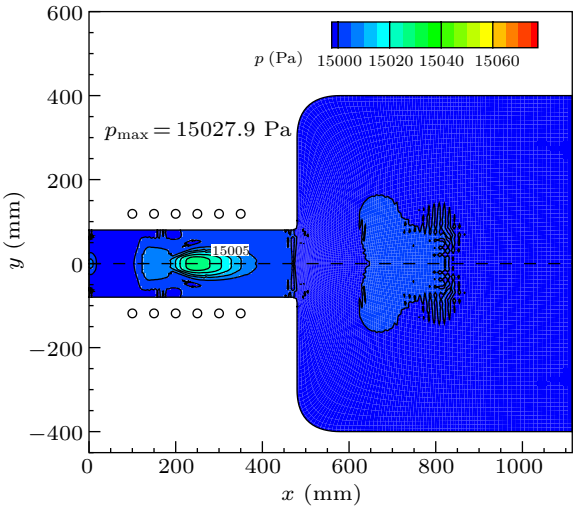


Fig. 12. Distribution of static pressure in the whole flow field for case 1.

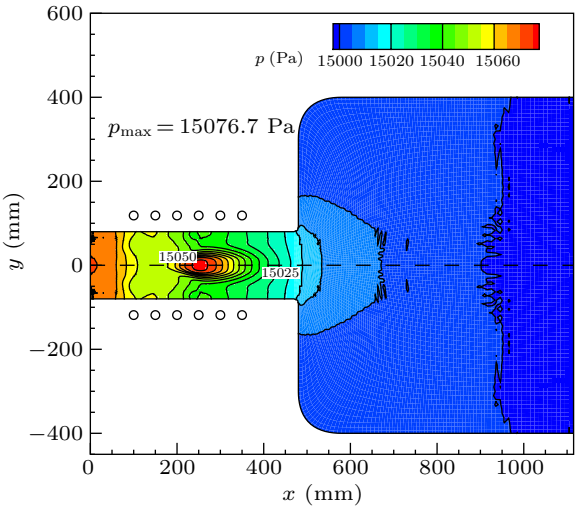


Fig. 13. Distribution of static pressure in the whole flow field for case 2.

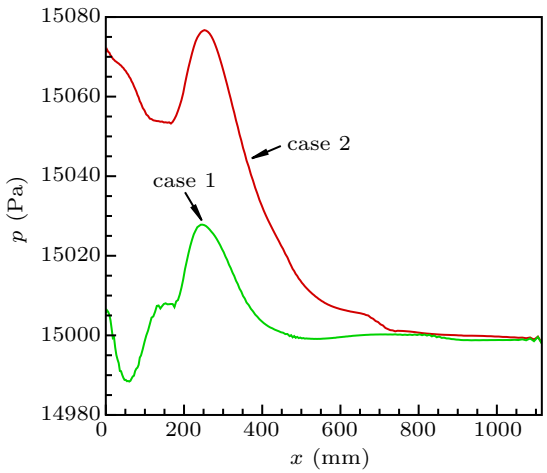


Fig. 14. Comparison of simulated static pressure along center axis between case 1 and case 2.

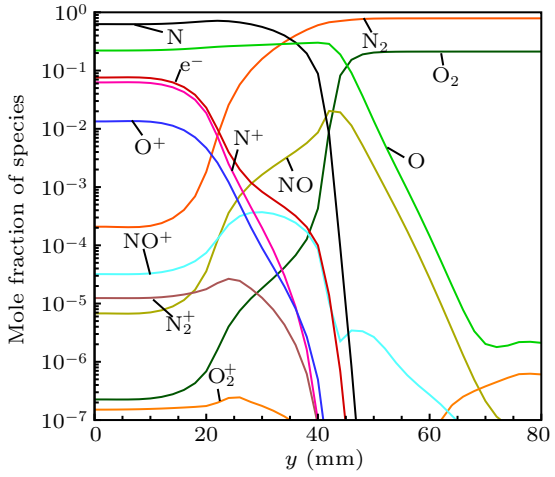


Fig. 15. Radial distribution of mole fractions for air species at the coil center $x = 225$ mm for case 1.

Figure 15 shows the radial distributions of mole fractions for air chemical species at the coil center $x = 225$ mm for case 1. As can be seen from the figure, the atomic N and O are the dominant chemical species before $y \leq 40$ mm. It indicates that in the vicinity of the central axis, after a series of dissociation and ionization reactions, nitrogen molecules decompose into atomic nitrogen N and ionic nitrogen N^+, oxygen molecules also decompose into oxygen atomic O and ionic oxygen O^+. The mole fractions of electrons e^- and ionic N^+ are about 0.1, and almost the same. That is to say, the negative charge of electrons just offsets the positive charge of ionic atomic nitrogen, so the simulated plasma flow is electrically quasi-neutral. With the increase of the distance from the central axis, the mole fractions of species N_2^+, O^+, N^+, e^-, NO^+ decrease fast after $y \geq 15$ mm. Molecular nitrogen becomes the main chemical species after $y \geq 40$ mm.

3.2. Experimental validation of simulated results

To validate the correctness of the numerical methods and the simulated results presented in this study, the quantitative comparisons between the simulated and the measured temperatures are performed. Four simulations listed in Table 1 are carried out according to the corresponding experimental study in the 1.2-MW ICP wind tunnel for comparison.

First, following the spectroscopic experimental study of Cipullo *et al.*,[24] the air inductive plasma jet produced by the 1.2-MW ICPWT is investigated. Intrusive and nonintrusive measurement technique are combined to characterize the plasma flow at a broad range of pressure and input power. The high speed camera imaging technique is used to study the flow features of the plasma, and a frequency-spatial-domain elaboration procedure is adopted to analyze the measured data. In the experiment, the high speed camera imaging is performed by using a complementary metal–oxide–semiconductor camera to ensure the complete visualization of the plasma flow field. Three spectrometers are used to observe the plasma at three different distances from the torch inlet ($x_1 = 665$ mm, $x_2 = 790$ mm, $x_3 = 915$ mm) along the central axis. The temperatures at these three positions are estimated by fitting the measured spectrum with the theoretical spectra.

Second, the simulated and measured temperatures are compared at these three positions for cases 1 and 3 ($P = 160$ kW), and cases 2 and 4 ($P = 200$ kW), respectively, in Figs. 16 and 17. In these two figures, the curves and the symbols denote the numerical and experimental results, respectively. Additionally, because the error range for cases 1 and 3 is not obtained in the experimental study,[24] none of the error bars of the experimental points are depicted in Fig. 16.

Third, as shown in Fig. 16, it can be observed that the temperature value sharply increases to a maximum and then slightly decreases in the plasma torch. Due to the strong external electromagnetic field generated by the electrified coil, the working gas entering from the inlet is heated rapidly by the electrified coil. So the gas temperature rises rapidly in the coil region. The simulated maximum temperatures for cases 1 and 3 are 10514 K and 10693 K, respectively. In addition, the measured (red circle and blue delta) and the simulated

(curves) temperatures in Fig. 16 decrease with the increase of the torch outlet distance due to the interaction between the plasma and its surrounding cold gas. In the vacuum chamber, the simulated temperatures accord well with the temperatures measured at the three positions. For example, at the position $x_3 = 915$ mm, the experimental and numerical temperatures for case 1 are 6108 K and 5941 K, respectively. The relative error between them is 2.7%.

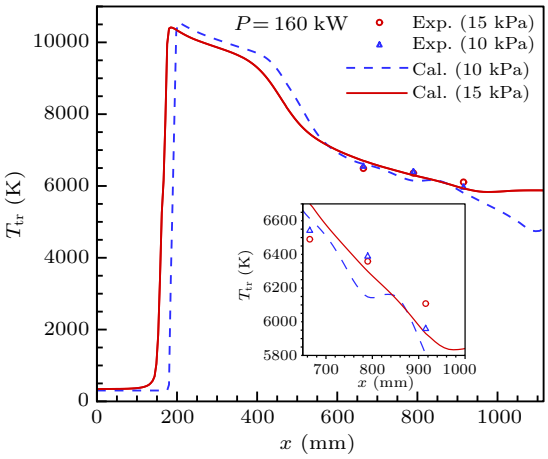


Fig. 16. Comparison between simulated and the measured temperatures along center axis for cases 1 and 3 ($P = 160$ kW).

Additionally, as can be seen in Fig. 16, the simulated temperatures show a slightly increasing tendency near the chamber outlet and in a region of 800 mm $\leq x \leq$ 880 mm for case 1 ($p = 15$ kPa) and case 3 ($p = 10$ kPa), respectively. This abrupt temperature fluctuation might be caused by uncertainties of chemical reactions of air in the simulation, because similar abrupt temperature increment and fluctuation were also found in the arc-heated air plasma simulation.[43] However, the fluctuation of the temperature simulated in our study is about 200 K. The relative error of the simulated temperature caused by this fluctuation is within 3.5%. So the effect of this temperature fluctuation might be ignorable. To make clear the definite reasons for this temperature fluctuation, this issue will be studied further in the future.

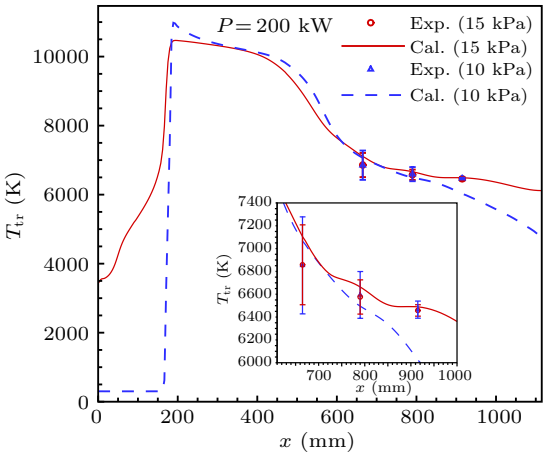


Fig. 17. Comparison between simulated and measured temperatures along center axis for cases 2 and 4 ($P = 200$ kW).

Finally, as shown in Fig. 17, generally the simulated and measured temperatures also accord well with each other in the test chamber. Although a few deviations can be seen at the position $x_3 = 915$ mm for the 10-kPa case (blue curve and blue symbol delta), the maximum relative error is 6.8%, because the measured and the simulated temperatures are 6465 K and 6024 K respectively. In summary, the maximum relative errors between the simulated and measured results for cases 1–4 are all within 6.8%, and thus indicating that the numerical methods and results presented in this study are reliable and suitable.

4. Conclusions

In this study, the basic flow and electromagnetic properties of a 1.2-MW high power ICP wind tunnel, such as its distribution of the temperature, pressure, electronic density, electric field intensity, Lorentz force, Joule heating rate, *etc*., are obtained by solving the multiphysics coupling fluid dynamic equations. The simulated temperatures are compared with the experimentally measured ones, and they accord well with each other. So the numerical methods used in this study are reliable and suitable.

Through the present study, it is also found that the maximum values of the temperature, pressure, electric field intensity, Lorentz force, Joule heating rate, and speed are all generated near the center of the induction coil. The temperature increases to the maximum value in the plasma torch, and then decreases with the increase in the distance from the torch outlet. The pressure value is kept basically the same in the test chamber, but slightly changes in the plasma torch. The change trend of the pressure is similar to that of the translational temperature. In addition, it is also observed that the maximum value of the radial Lorentz force is practically twice or thrice bigger than that that of the axial the Lorentz force. As a result, the momentum transfer in the radial direction is stronger. Moreover, the movement of electrons is also strongly affected by the radial Lorentz force pointing to the central axis. The electron number density and positive electric field intensity generated by the electron are largest at the central axis. Consequently, the negative electric-field intensity generated by the coil current is partially offset by the positive electric field intensity generated by electrons. At the entrance of the torch and near the wall of the test chamber, it is found that the eddy flows are easily produced.

Acknowledgment

All simulations were performed by using the Tianhe-2 Supercomputer at the National Supercomputer Center in Guangzhou, China.

References

[1] Liu L, Wang, G, Wang Y, Ma H, Luo J and Zhang J 2017 *Acta Aeronaut. Astronaut. Sin.* **38** 96 (in Chinese)
[2] Ma H, Wang G, Luo J, Liu L, Pan D, Zhang J, Xing Y and Tang F 2018 *Acta Phys. Sin.* **67** 186 (in Chinese)
[3] Wei X L, Xu H J, Li J H, Lin M and Song H M 2015 *Acta Phys. Sin.* **64** 175201 (in Chinese)
[4] Moon J, Kim K, Lin M and Chung C 2016 *Phys. Plasmas* **23** 113504
[5] Kim K, Kim K, Hong Y, Moon H and Chung C 2019 *Phys. Plasmas* **26** 123516
[6] Pan D, Jiang G, Wang G, Ma H, Liu L and Luo J 2014 *J. Exper. Fluid Mech.* **28** 72 (in Chinese)
[7] Fujita K, Mizuno M, Ishida K, and Ito T 2008 *J. Thermophys. Heat Transfer* **22** 685
[8] Ivanov D V and Zverev S G 2017 *IEEE T. Plasma Sci.* **45** 3125
[9] Degrez G, Abeele D V, Barbante P and Bottin B 2004 *Int. J. Numer. Method Heat Fluid Flow* **14** 538
[10] Alavi S and Mostaghimi J 2019 *Plasma Chem. Plasma Proc.* **39** 359
[11] Nam J, Lee M, Seo J and Kim G 2018 *J. Korean Phys. Soc.* **72** 755
[12] Lu B and Feng Q 2018 *Phys. Plasmas* **25** 093510
[13] Sun X Y, Zhang Y R, Chai S, Wang Y N, Chu Y Y and He J X 2020 *Chin. Phys. B* **29** 095203
[14] Sun X Y, Zhang Y R, Li X C and Wang Y N 2017 *Chin. Phys. B* **26** 015201
[15] Gao F, Zhang Y R, Zhao S X, Li X C and Wang Y N 2014 *Chin. Phys. B* **23** 115202
[16] Zhu H, Tong H, Ye G and Chen L 2012 *Nucl. Fusion Plasma Phys.* **32** 199 (in Chinese)
[17] Chen W, Chen L, Liu C, Chen C, Tong H and Zhu H 2019 *High Volt. Eng.* **45** 316 (in Chinese)
[18] Zhao S 2018 *Phys. Plasmas* **25** 033516
[19] Lei F, Li X, Liu D, Liu Y and Zhang S 2019 *AIP Adv.* **9** 085228
[20] Kralkina E A, Rukhadze A A, Pavlov V B, Vavilin K V, Nekliudova P A, Petrov A K and Alexandrov A F 2016 *Plasma Sources Sci. T.* **25** 015016
[21] Yu B W and Girshick S L 1991 *J. Appl. Phys.* **69** 656
[22] Yu, M H, Yamada, K, Takahashi, Y, Liu, K and Zhao T 2016 *Phys. Plasmas* **23** 123523
[23] Xue S, Proulx P and Boulos M I 2003 *Plasma Chem. Plasma P.* **23** 245
[24] Cipullo A, Helber B, Panerai F, Zeni L and Chazot O 2014 *J. Thermophys. Heat Transfer* **28** 381
[25] Vasil'eviskii S A and Kolesnikov A F 2000 *Fluid Dynam.* **35** 769
[26] Sumi T, Fujita K, Kurotaki T, Ito T, Mizuno M and Ishida K 2005 *Trans. Jpn. Soc. Aeronaut. Space Sci.* **48** 40
[27] Abeele D V and Degrez G 2004 *Plasma Sources Sci. Technol.* **13** 680
[28] Gupta R N, Yos J M, Thompson R A and Lee K P 1990 *A review of reaction rates and thermodynamic and transport properties for an* 11-*species air model for chemical and thermal nonequilibrium calculations to* 30000 K (Washington DC: National Aeronautics and Space Administration) pp. 1–91
[29] Yos J M 1963 *Transport properties of nitrogen, hydrogen, oxygen, and air to* 30000 K, (Wilmington, Massachusetts: Research and Advanced Development Division, AVCO Corporation) pp. 1–71
[30] Curtiss C F and Hirschfelder J O 1949 *J. Chem. Phys.* **17** 550
[31] Devoto R S 1967 *Phys. Fluids* **10** 2105
[32] Yu M, Kihara H, Abe K and Takahashi Y 2015 *J. Korean Phys. Soc.* **66** 1833
[33] Ghorui S and Das A K 2013 *Phys. Plasmas* **20** 093504
[34] Yu M, Wang W, Yao J and Zheng B 2018 *J. Korean Phys. Soc.* **73** 1519
[35] Park C 1990 *Nonequilibrium Hypersonic Aerothermodynamics* (New York: Wiley) pp. 1–358
[36] Shima E and Kitamura K 2011 *AIAA J.* **49** 1693
[37] Van Leer B 1979 *J. Comput. Phys.* **32** 101
[38] Van Leer B 1977 *J. Comput. Phys.* **23** 276
[39] Bussing T R A and Murman E M 1988 *AIAA J.* **26** 1070
[40] Jameson A anYoon S 1987 *AIAA J.* **25** 929
[41] Chen X 1990 *Int. J. Heat Mass Transfer* **33** 815
[42] Ivanov D V and Zverev S G 2020 *IEEE T. Plasma Sci.* **48** 338
[43] Takahashi Y, Kihara H and Abe K 2010 *J. Thermophys. Heat Transfer* **24** 31